Journal of Metals, Materials and Minerals, Vol. 31, No. 4, pp. 62-68, 2021

Structural, magnetic and transport properties of Ca and Sr doped Lanthanum manganites

Sunita KESHRI[1], Shailendra RAJPUT[2,*], Sonali BISWAS[1], Leena JOSHI[3], Wojciech SUSKI[4], and Piotr WIŚNIEWSKI[4]

[1] *Department of Physics, Birla Institute of Technology, Mesra, RANCHI, 835215, INDIA*
[2] *Department of Physics, Shri Krishna University, CHHATARPUR, 471001, INDIA*
[3] *Department of Physics, St. Xavier's College Bombay, MUMBAI, 400001, INDIA*
[4] *Institute of Low Temperature and Structure Research, Polish Academy of Sciences, P.O. Box 1410, WROCLAW 2, 50-950, POLAND*

***Corresponding author e-mail:** shailendra.phy@gmail.com

Received date:
17 June 2021
Revised date
11 September 2021
Accepted date:
5 October 2021

Keywords:
Manganite;
Resistivity;
M-I transition;
Magnetization;
Thermoelectric power

Abstract

This article presents a comparative study for the effect of average A-site cation size on the structural, transport and magnetic properties of Lanthanum manganites. Three polycrystalline colossal magneto-resistive compounds were synthesized using standard solid state reaction method. The electrical resistivity data were analyzed employing standard two-phase model to understand the conduction mechanism. The resistance of polycrystalline ceramic depends on the intragrain resistance (intrinsic resistance) and the intergrain or grain-boundary resistance (extrinsic resistance). The substitution of Sr ions at La-site provides higher magnetic and metal-insulator transitions as compared to Ca ions. The combined substitution of Ca and Sr ions at La-site offers nearby room temperature magnetic and metal-insulator transitions. Irreversibility in the temperature dependent DC magnetization is observed in the zero-field-cooled and field-cooled measurements. It is noticed that the larger average radius of the A-site cations possesses higher magnetic and metal-insulator transition temperatures. Temperature dependent thermoelectric power curves show a hump like behavior, which indicates a smooth transition from the low-temperature metallic behavior to high-temperature semiconductor-like behavior.

1. Introduction

Colossal Magnetoresistance (CMR) effect in the manganites has attracted widespread attraction of research community because of their interesting physical properties [1-5]. The perovskite manganites of general formula $R_{1-x}A_x\mathrm{MnO_3}$ (where R is trivalent rare earth ion and A is alkaline earth element) are found to possess significant CMR effect [1,2]. In addition to this, these materials show specific features of ferromagnetic-paramagnetic phase transition, and metal-insulator transition. The interest in CMR materials was reinforced due to their specific technological applications such as spintronic devices, magnetic recording media, magnetic sensors, permanent magnets etc. These materials also exhibit a high Seebeck coefficient (also known as thermoelectric power), because the $4f$ levels in these compounds situate nearby the Fermi energy and create large density of states at the Fermi level [6]. A systematic analysis of its data provides information about the conduction mechanisms. Also, thermoelectric power of the manganites needs to be explored in view of the green energy candidates.

The characteristic behavior of $\mathrm{La_{1-x}A_xMnO_3}$ manganites strongly depends on the concentration of substitution at La-site [1-6]. The mixed valence state of Mn ions (Mn^{3+} and Mn^{4+}) is induced by the substitution of divalent or trivalent cations at La-site. The manganites exhibit metal-insulator (M-I) transition temperature (T_{MI}) and paramagnetic to ferromagnetic transition at Curie temperature (T_C) [7]. The conduction mechanism of the manganites can be explained in terms of two types of CMR effects: intrinsic and extrinsic [5]. In general, the intrinsic CMR effect is noted in the vicinity of intrinsic M-I transition and T_C [3], and it can be explained using the double exchange (DE) interaction mechanism between Mn^{3+} and Mn^{4+} ions [8]. The DE mechanism is also responsible for the occurrence of ferromagnetism. In addition to the DE mechanism, the strong electron-phonon interaction arising from Jahn-Teller splitting should also be considered for the observed CMR effect [9]. On the other hand, the extrinsic CMR effect is related to the natural and artificial grain boundaries and identified by a broad M-I transition [10,11]. The extrinsic M-I transition temperature is always lower than that of intrinsic one. The extrinsic CMR effect is originated from the spin polarized tunneling among adjacent grains [12,13]. Several fundamental questions have been raised regarding the conductivity mechanisms in CMR materials as magnitude of resistance changes significantly with the application of magnetic field. Previous studies proposed different models for conduction mechanism in the paramagnetic phase [14-19]. In general, it is noted that the presence of small polarons plays a key role in the unusual transport properties of manganites. However, an open question about the precise transport process of small polarons remains unanswered. It is a matter of dispute and demands further investigations.

In this article, the effect of average A-site cation size on the transport and magnetic properties of $\mathrm{LaMnO_3}$ is studied. The $\mathrm{La_{0.67}Ca_{0.33}MnO_3}$ (LCMO), $\mathrm{La_{0.7}Ca_{0.2}Sr_{0.1}MnO_3}$ (LCSMO), and $\mathrm{La_{0.67}Sr_{0.33}MnO_3}$ (LSMO) compositions were grown for this investigation.

2. Experimental

Polycrystalline samples of LCMO, LCSMO and LSMO were prepared by the conventional solid-state route. The stoichiometric amount of La_2O_3, $CaCO_3$/$SrCO_3$ and $Mn(CH_3COO)_2{\cdot}4H_2O$ were taken. The starting compositions were first fired at 900°C for 24 h and then at 1100°C for 18 h with intermediate grindings. The powder thus obtained was pelletized and sintered at 1250°C for 12 h with intermediate grinding and re-pelletization, and finally furnace cooled to room temperature. The DC electrical resistivity as a function of temperature down to 10 K was measured by the standard four probe method using a closed cycle Helium-cryostat (Oxford Instruments Ltd). The AC susceptibility measurements were carried out with the variation of temperature down to 10 K, using a lock-in-amplifier (Stanford Research, SR-530). The zero-field-cooled (ZFC) and field-cooled (FC) magnetization measurements have been done at 10 Oe DC field using a SQUID magnetometer (Quantum Design, MPMS-5). The temperature-dependent thermoelectric power (TEP) measurements were carried out by a differential method with a constant gradient of 2 K.

3. Results and discussion

The XRD data were analyzed by the Rietveld refinement method [20] employing FullProf Suite program [21]. Figures 1(a-c) demonstrate typical refined XRD patterns of LCMO, LCSMO and LSMO ceramics. Refinement analysis yields an excellent agreement between the experimental (I_{obs}) and calculated (I_{cal}) diffraction profiles of grown ceramics. The XRD patterns confirm the formation of single-phase ceramics, as impurity or un-reacted phases are not observed. The LCMO and LCSMO samples confirm the orthorhombic crystal structure with *Pbnm* space group, while LSMO sample exhibits the rhombohedral structure with $R\bar{3}c$ space group. The unit cell parameters and crystallographic data are summarized in Table 1. It is observed that the unit cell parameters increase with an increasing average radius of A-cations, which is in agreement with the previous reports [22,23]. The observed behavior might be attributed to the fact that the substitution of a larger ion expands the unit cell in all three directions enhancing its volume. It is also noticed that the Mn-O(1) bond length decreases and average Mn-O(2) bond length increases, which indicates an attenuation in Jahn-Teller distortion of MnO_6 with increasing A-site ionic radii. This distortion plays an important role in determining the magnetic and transport properties of mixed-valence manganites [24]. The *Pbnm* and *Pnma* space groups allow three independent Mn-O bonds and therefore, can accommodate a distortion. We find that the substitution by Ca^{2+}causes minimum lattice distortion in the MnO_6 octahedra, possibly due to the smaller ionic radius of Ca^{2+} (0.100 nm) than that of La^{3+} (0.103 nm), whereas ionic radius of Sr^{2+} is slightly larger (0.118 nm) as compared to the ionic radius of La^{3+} [25].

The SEM micrographs and EDX spectra of LCMO, LCSMO and LSMO are shown in Figures 2(a-f). It can be observed from the figures that various sizes of grains are randomly distributed, but the grains of all samples are distinct and have well-defined boundaries. The grain sizes of LCMO, LCSMO and LSMO phases lie in the range of ~6 μm to 7 μm, 2 μm to 4 μm, and 4 μm to 8 μm respectively. The Au peaks in the EDX spectra come from the coating of gold over the surface of sample to avoid charging. From EDX results, it is clear that the samples contain all the compositional elements in proportions close to the desired values.

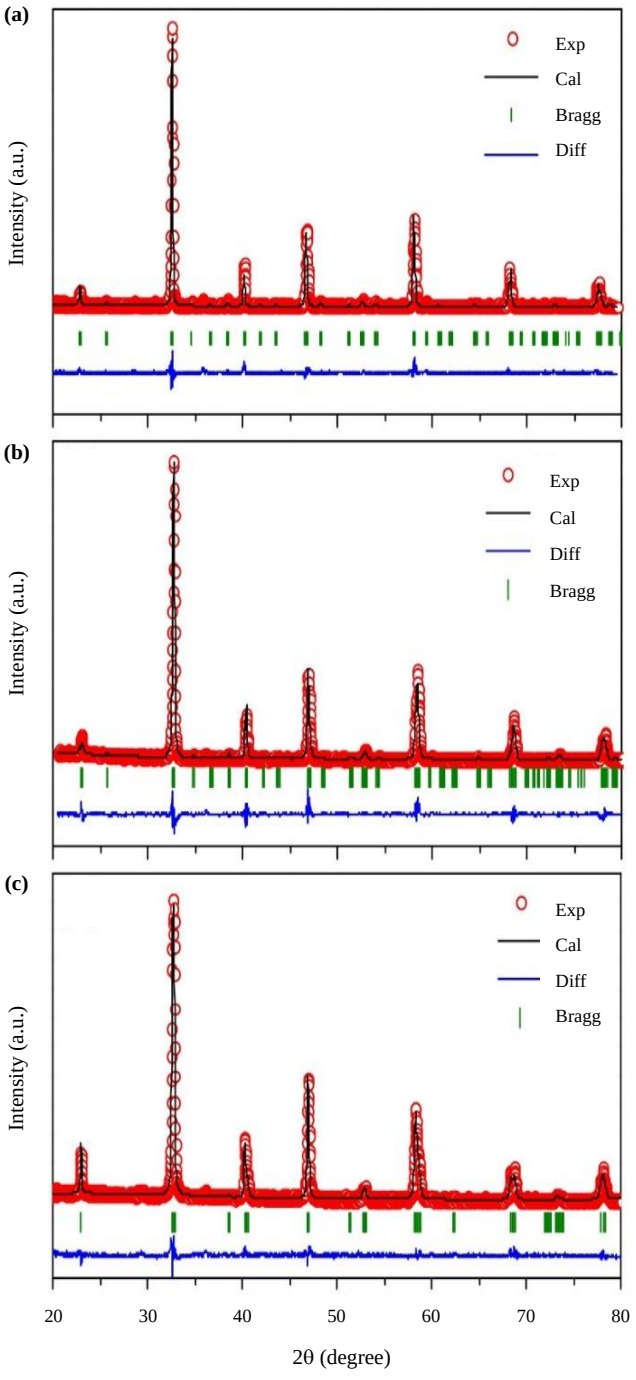

Figure 1. Experimental (open symbols) and calculated (solid lines) X-ray diffraction patterns for (a) LCMO, (b) LCSMO, and (c) LSMO manganites. Positions for the Bragg reflections are marked by vertical bars. Differences between the observed and the calculated intensities are shown at the bottom of the figure.

Table 1. Lattice parameters, bond angles, bond lengths, structure types and Rietveld refinement parameters for LCMO, LCSMO and LSMO samples.

Sample	$La_{0.67}Ca_{0.33}MnO_3$	$La_{0.7}Ca_{0.2}Sr_{0.1}MnO_3$	$La_{0.67}Sr_{0.33}MnO_3$
Sample code	LCMO	LCSMO	LSMO
Structure	Orthorhombic	Orthorhombic	Rhombohedral
Space group	*Pnma*	*Pbnm*	$R\bar{3}c$ (hexagonal axes)
Z (f.u./cell)	4	4	6
a (Å)	5.4705(2)	5.4734(1)	5.4882(2)
b (Å)	7.7049(3)	5.4682(3)	5.4882(2)
c (Å)	5.4511(3)	7.7249(2)	13.3443(3)
Volume (Å^3)	229.998	232.2141	348.0594
Volume/f. u. (Å^3)	57.4995	58.0535	58.0099
R_P	32.0	24.6	22.0
R_{WP}	40.7	21.3	14.9
R_{EXP}	31.4	12.3	12.8
R_{Bragg}	15.7	11.2	6.05
χ^2	1.69	2.69	1.36
$d_{Mn\text{-}O1}$ (Å)	2.0686	1.9503	1.9459
$d_{Mn\text{-}O2}$ (Å)	1.9617	1.9739	--
$\theta_{Mn\text{-}O1\text{-}Mn}$	158.184°	158.1734°	168.2113°
$\theta_{Mn\text{-}O2\text{-}Mn}$	166.063°	163.9747°	--

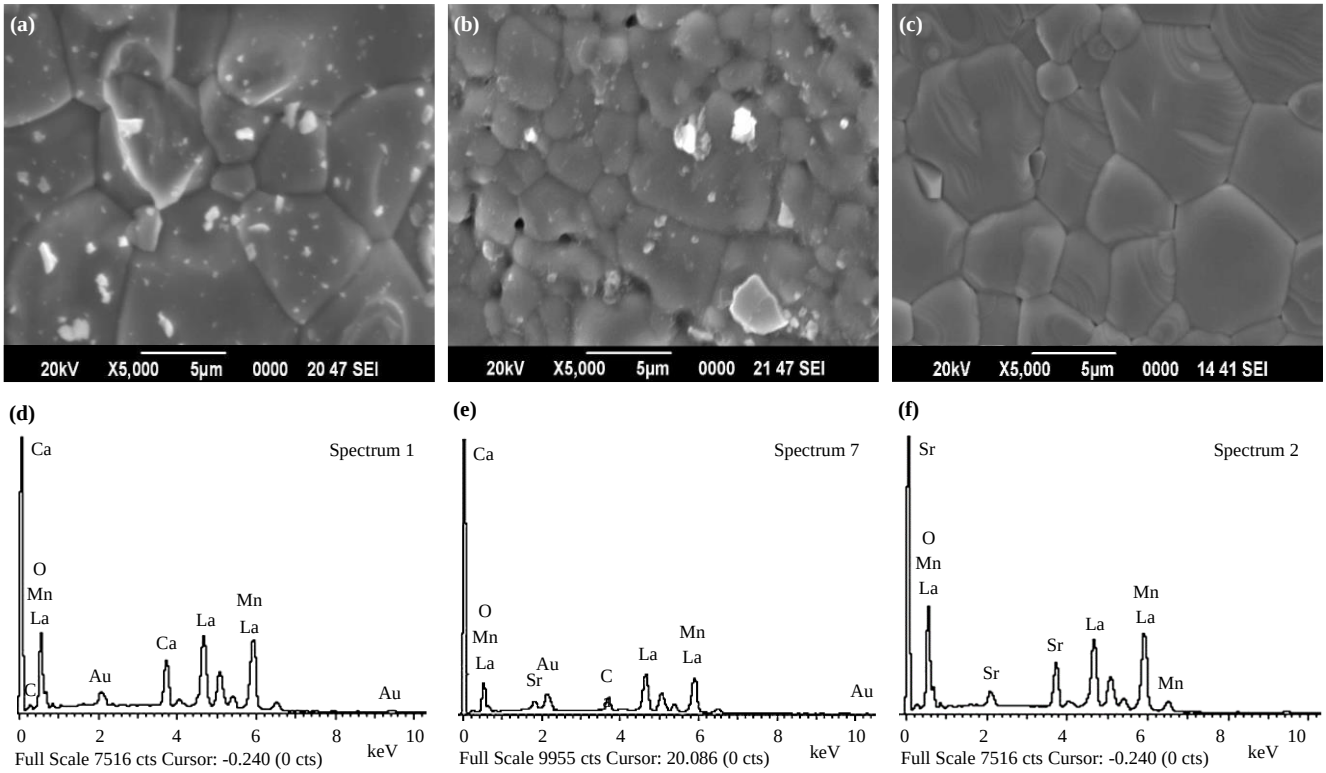

Figure 2. SEM micrographs of (a) LCMO, (b) LCSMO, and (c) LSMO samples. The corresponding EDX patterns of (d) LCMO, (e) LCSMO, and (f) LSMO samples.

Figures 3 (a-c) represent the electrical resistivity of these samples as a function of temperature. All the samples show distinct M-I transition, which is found to be a strong function of the substituting ions at La-site, the values of T_{MI} are listed in Table 2. This is because of the fact that the distortion of MnO_6 octahedra affects the transition temperature in manganites [26]. It is well known that grain boundaries play an important role in determining the transport behavior of poly-crystalline samples. Total resistance of any polycrystalline ceramic depends on the nature of grain boundaries and grain connectivity. It consists of the intragrain resistance (intrinsic resistance) and the intergrain or grain-boundary resistance (extrinsic resistance). The ideal intrinsic magnetic and transport properties are achieved within the grain. These properties result out in the simultaneous occurrence of (intrinsic) M-I and PM-FM transitions governed by the DE mechanism. On the other hand, the extrinsic properties result in a broad (extrinsic) M-I transition, which occurs at a temperature of $T_{MI} < T_C$. It is generally ascribed to the spin-polarized inter-grain tunneling across the interfaces or grains. The grain boundaries are magnetically disordered mainly because of oxygen vacancies and broken Mn-O-Mn bonds. The intrinsic M-I transitions for LCMO and LCSMO samples are found

at 260 and 304 K, respectively. However, the LSMO sample shows extrinsic M-I transition at 282 K. Lu *et al.* [27] have found an intrinsic M-I transition at ~365 K followed by a hump for LSMO nanomaterials.

The analysis of the transport mechanism involved in the temperature dependent resistivity behavior, has been carried out with the help of the two-phase percolation model. The results show that the resistivity data in FM metallic region are governed by the electron-scattering process and fitted by the following equation [28]:

$$\rho_{FM} = \rho_0 + \rho_2 T^2 \quad (1)$$

where ρ_0 is the residual resistivity due to the domains, grain boundaries, and other temperature independent scattering mechanism whereas the $\rho_2 T^2$ term represents the combined effect of the electron-electron scattering, electron-phonon scattering and electron-magnon scattering. Insulating PM phase is dominated by the hopping motion of the self-trapped small polarons. The resistivity in this region can be fitted well by the following equation:

$$\rho_{FM} = \rho_\alpha \, Texp\,(E_A / k_B T) \quad (2)$$

where ρ_α is a constant, E_A is the activation energy, and k_B is Boltzmann constant [29; references therein].

Unfortunately, none of the above models are able to explain the prominent change of the resistivity nearby T_C. Based on the phase-segregation mechanism (percolation model) [28,30], we have approximated that the FM cluster and PM regions coexist in CMR materials. The resistivity at any temperature is related to the change of the volume fractions of the both regions. Under this circumstance, the resistivity for the entire temperature range may be expressed as:

$$\frac{1}{\rho} = \frac{(1-f)}{\rho_{PM}} + \frac{f}{\rho_{FM}} \quad (3)$$

where ρ_{PM} and ρ_{FM} are the resistivities of the PM, and FM contents in the sample [31]. Combination of Equations (1) and (2) with Equation (3) provides us:

$$\frac{1}{\rho} = \frac{(1-f)}{\rho_\alpha Texp(E_A/k_B T)} + \frac{f}{\rho_0 + \rho_2 T^2} \quad (4)$$

The functions $(1 - f)$ and f are the volume fractions of PM and FM phases respectively. The function f is expressed as:

$$f = 1/[1 + exp\{\Delta U / k_B T\}] \quad (5)$$

where ΔU is the energy difference between the FM and PM states and volume fraction. It is expressed as: $\Delta U \sim -U_0 (1 - T/T_C^{mod})$. In this expression, T_C^{mod} is considered as a theoretical value of T_C. The ground is the FM state which is of lower energy than insulating state, hence in this expression $-U_0$ is taken as the maximum energy difference for temperature region well below transition temperature. In Figure 3, the solid lines represent the fitting results for the resistivity curves for LCMO, LCSMO and LSMO samples. It can be observed that the results calculated from Equation (3) agree well with the experimental data; the best-fit parameters are listed in Table 2. The T_C^{mod} is observed to be smaller than experimental T_C [listed in Table 2].

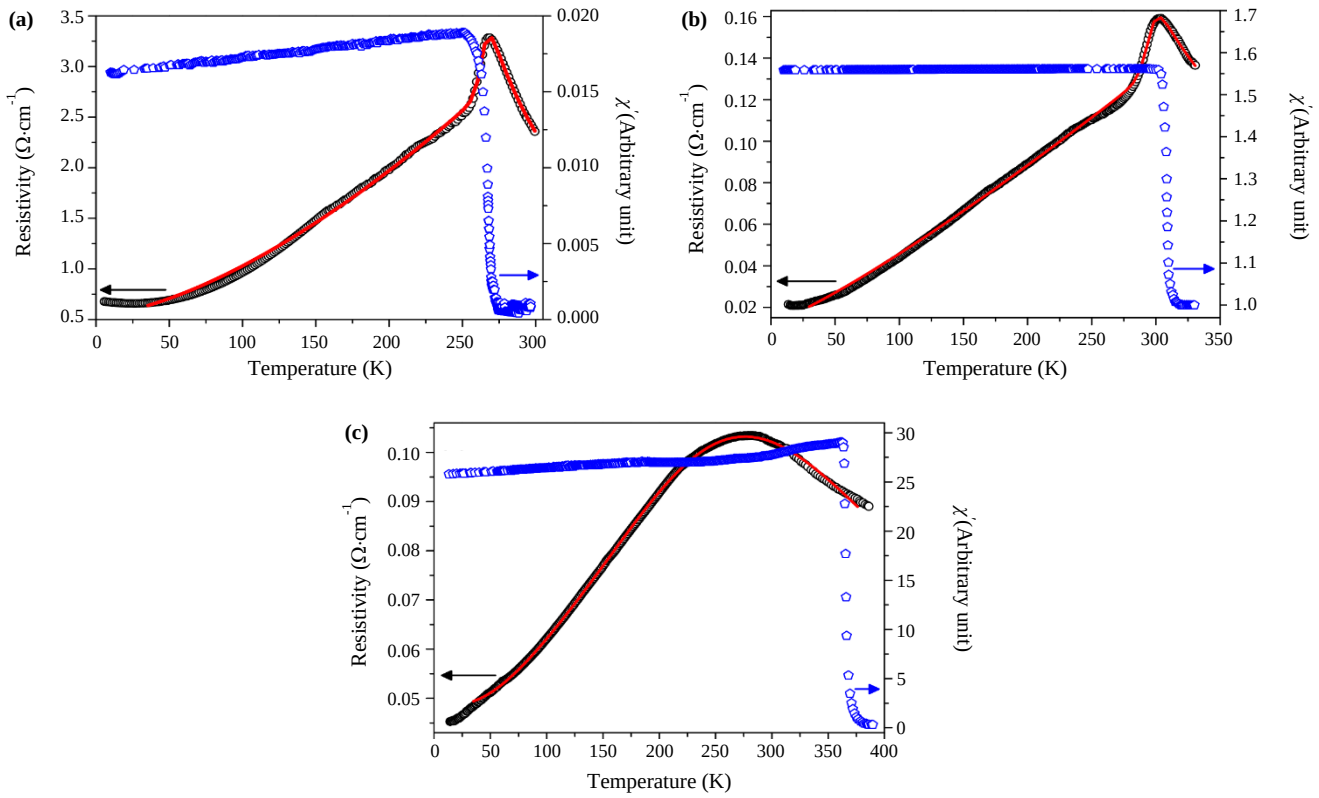

Figure 3. Temperature variation of resistivity and AC susceptibility of (a) LCMO, (b) LCSMO, and (c) LSMO samples. In resistivity curves, solid lines represent the theoretical curves obtained using two phase model.

Table 2. Parameters obtained by fitting with Equation (4) and the transition temperatures.

Sample	ρ_0 (Ω-cm)	ρ_2 (Ω-cm·K^{-2})	ρ_α (Ω-cm)	E_A/k_B (K)	U_0/k_B (K)	T_C^{mod} (K)	T_{MI} (K)	T_C from $\chi'(T)$ (K)	T_C from $M(T)$ (K)
LCMO	0.54052	0.00039	0.00013	1224.58	28997.92	263.69	266	268	269
LCSMO	0.01236	0.00014	0.00002	1453.69	23435.60	294.78	304	309	309
LSMO	0.03812	2.9532E-7	5.796E-6	1507.13	246.16	327.58	282	365	369

A systematic study of the AC magnetic susceptibility as a function of temperature has been carried out, for all the samples. The temperature versus AC magnetic susceptibility curves are shown in Figures 3(a-c). The frequency of AC signal has been kept constant at 131 Hz during the experiment. The T_C is determined from the minimum point of $(d\chi'/dT)$ versus temperature plot. The magnetic transition temperature values have been found to be 268, 309, and 365 K for LCMO, LCSMO, and LSMO samples, respectively (Table 2). It is concluded that the substitution of La^{3+} of by Sr^{2+} gives higher T_C compared to the substitution by Ca^{2+}. This is because of the fact that the ionic radius of La^{3+} (~0.103 nm) is smaller than the radius of Sr^{2+} (~0.118 nm) and larger than that of Ca^{2+} (~0.100 nm). The average ionic radius of the La site increases with the substitution by Sr^{2+} ion, which thereby introduces a crystallographic distortion and enhances the Mn-O-Mn bond angle. In the framework of the double-exchange interaction theory, a shorter Mn-O distance (larger Mn-O-Mn bond angle) leads to a stronger interaction and consequently higher T_C [32]. The values of T_C for LCMO and LCSMO are comparable with their corresponding T_{MI} values; whereas for LSMO, $T_{MI} < T_C$ as it shows extrinsic behavior. It is observed that at low temperature, the susceptibility curve shows a small downturn indicating the presence of FM phase with a possible amount of anti-ferromagnetic phase. This can be attributed to the fact that at grain boundaries, DE (Mn^{3+}-O-Mn^{4+}) and super exchange (Mn^{3+}-O-Mn^{3+} and (Mn^{4+}-O-Mn^{4+}) interactions are weak as compared to those inside the grain. The grain boundary effect becomes more prominent in the low temperature region and causes an inhomogeneity in the magnitude of the exchange interactions, resulting in a downturn in $\chi'(T)$ curve at low temperatures.

Figure 4 shows the normalized FC and ZFC magnetization curves of the samples, measured under 10 Oe DC magnetic field. The transition temperature values are obtained by considering the peak value of the derivative of M (i.e. dM/dT) verses T plot. The T_C values are obtained as 266, 309 and 369 K for LCMO, LCSMO and LSMO respectively (listed in Table 2). Similar results have been obtained from the susceptibility measurement also. The irreversibility in the temperature dependence of ZFC and FC magnetizations is found for all three samples. This phenomenon shows evidence of granular ferromagnets. For these manganites, the long-range orderly an arrangement of Mn-O-Mn is destroyed and Mn-O-Mn forms clusters. Upon zero-field cooling, the clusters freeze into random orientations and the response depends on the competition between the random local magnetization orientations of the individual clusters and the applied magnetic field. When cooling is done in the presence of a field, the clusters align, and a large ferromagnetic-type magnetization arises. The irreversibility decreases with the increase in temperature and vanishes as the ZFC magnetization curves coincide with FC magnetization curves, displaying a FM to PM transition at the Curie temperature.

Figure 5 represents the thermal variation of the thermoelectric power (S) of the grown ceramics. The LCMO sample shows negative values of TEP for the entire temperature range, which suggests the dominance of electrons in thermoelectric transport. Unlike the electrical resistivity, thermoelectric power shows hump like behavior which indicates that the samples show a smooth transition from the low-temperature metallic behavior to the high-temperature semiconductor-like behavior (1/T). For LCSMO sample, the TEP value is negative near room temperature and it shows a crossover from negative to positive at a temperature of ~221 K and remains positive for the low temperature region. It indicates the change in nature of charge carriers from electron-to hole-like behavior. For LSMO, the TEP value is positive for the temperature range of 140 to 244 K and remains negative for other temperatures. It may be mentioned that similar behavior was observed for $Pr_{2/3}(Ba_{1-x}Cs_x)_{1/3}MnO_3$ manganites [33]. For Sr doped samples, the lattice distortion increases because of the different ionic radius of La^{3+} and Sr^{2+} ions. Therefore, higher lattice distortion leads to the smaller e_g-electron bandwidth, which results in the localization of the charge carriers. This effect might be related to the positive magnitudes of TEP, in case of Sr^{2+} rich manganites.

In the metallic regime ($T < T_{MI}$), S has been analysed using the following equation:

$$S = S_0 + S_{3/2}T^{3/2} + S_4T^4 \quad (6)$$

where the term S_0 accounts for the problem of truncating the low temperature data and $S_{3/2}T^{3/2}$ is attributed to electron–magnon scattering process [34,35]. The term S_4T^4, dominant in high temperature region near T_{MI}, is thought to arise from the spin–wave fluctuations in the FM phase [34,24]. It is observed that the magnitude of $S_{3/2}$ is nearly six orders of magnitude larger than that of S_4 (Table 3). It means that

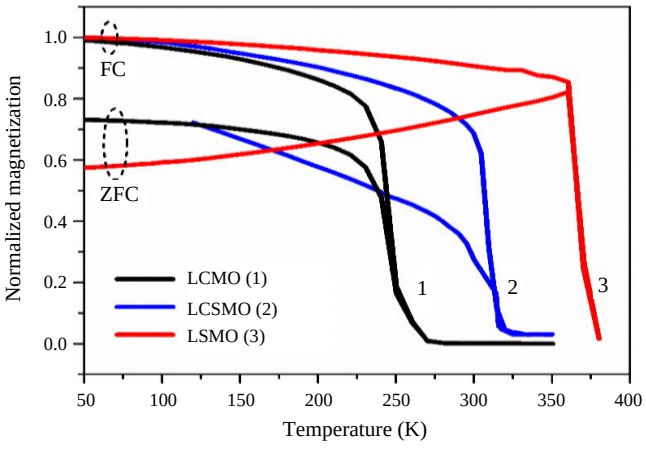

Figure 4. Temperature variation of DC magnetization ZFC, and FC conditions (1-LCMO, 2-LCSMO, 3-LSMO).

Table 3. Fitting parameters obtained by fitting TEP data with Equations (6) and (7).

Sample	Temp. range (K)	S_0 (μV/K)	$S_{3/2}$ (μV/K$^{5/2}$)	S_4 (μV/K^5)	Temp. range (K)	E_S / k_B	α	T_{MI} from TEP (K)	E_A / E_S (meV)
LCMO	100-270	-6.796 ± 0.073	0.005 ± 0.000	-4.678E-9 ± 3.026E–11	267-335	57.900 ± 0.093	-0.331 ± 0.000	267	100.53
LCSMO	100-270	0.093 ± 0.023	0.002 ± 0.000	-2.286E-9 ± 1.076E–11	270-299	86.007 ± 0.358	-0.380 ± 0.001	270	117.78
LSMO	100-285	-2.119 ± 0.013	0.001 ± 0.000	-9.645E-10 ± 4.873E-12				~360	

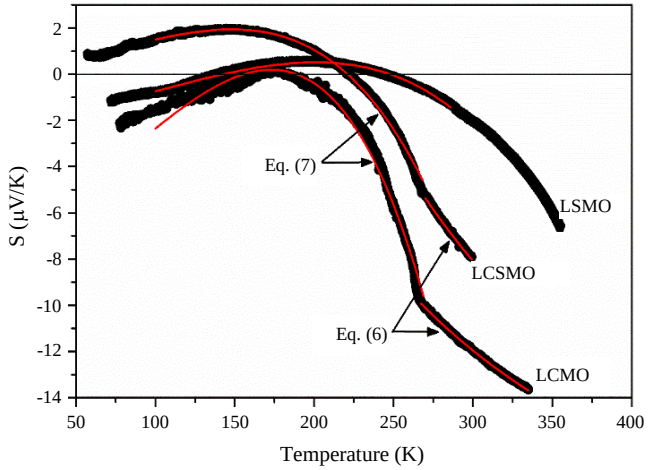

Figure 5. Thermoelectric power (S) of LCMO, LCSMO and LSMO samples with variation of temperature. Solid lines represent the theoretical fitting data using Equation (6) and (7).

the electron–magnon scattering (represented by $S_{32}\,T^{3/2}$) dominates the transport mechanism in the FM metallic regime. The occurrence of the electron–like TEP at high temperature is due to the fact that $S_4 < 0$. At higher temperatures, the term $S_4\,T^4$ dominates because of the larger magnitude and higher order of T.

If conduction due to spin polaron hopping (SPH) dominates the carrier transport in the insulating region (above T_{MI}), then $S(T)$ should follow the following relation [34]:

$$S(T) = (k_B/e)\left[\frac{E_S}{k_B T} + \alpha\right] \qquad (7)$$

where E_S is the activation energy obtained according to the fitting of the $S(T)$ data and α is a constant related to the kinetic energy of the polarons [35]. At least two conditions should be fulfilled for the SPH conduction: $\alpha < 1$, and $E_S < E_A$, where E_A is the activation obtained from the fitting of $\rho_{PM}(T)$ data. The fitting of high temperature TEP data using Equation (7) is also shown in Figure 5 and the fitting parameters (α and E_S) are listed in Table 3. The obtained α values are found to be less than one, which means that the SPH dominates the carrier transport in these CMR materials. Moreover, the magnitude of E_S is much smaller than that of E_A, which is the characteristic of SPH. The value of $(E_A - E_S)$ is also listed in Table 3, which is found to be greater for LCSMO compared to that for LCMO.

4. Conclusions

The influence of cation mismatch on transport and magnetic properties of Ca and Sr doped lanthanum manganites, LCMO, LCSMO and LSMO, has been reported in this paper. Using the Rietveld refinement technique, the LCMO and LCSMO samples are found to have the orthorhombic structure with *Pbnm* space group whereas the LSMO has rhombohedral structure with $R3\bar{c}$ space group. Resistivity data of these samples have been analyzed using the two-phase model. The values of T_C obtained by AC susceptibility as well as DC magnetization measurement indicate that the increase in the average radius of the A-site cations causes an increase in T_C. The LCMO and LCSMO samples show intrinsic CMR behavior and for them $T_C \sim T_{MI}$. However, LSMO shows M-I transition of extrinsic nature and $T_{MI} < T_C$ for it. Large difference between ZFC and FC data indicates strong domain effects in these materials. The hump like behavior of TEP indicates that the samples show a smooth transition from the low-temperature metallic behavior to the high-temperature semiconductor-like behavior.

Acknowledgements

The authors are thankful to the members of Central Instrumentation Facility Lab, Birla Institute of Technology, Mesra for providing SEM and EDX facilities.

References

[1] Y. Tokura, "Critical features of colossal magnetoresistive manganites," *Reports on Progress in Physics*, vol. 69, p. 797, 2006.

[2] C. B. Larsen, S. Samothrakitis, A. D. Fortes, A. O. Ayaş, M. Akyol, A. Ekicibil, and M. Laver, "Basal plane ferromagnetism in the rhombohedral manganite $La_{0.85}Ag_{0.15}MnO_{3+\delta}$," *Journal of Magnetism and Magnetic Materials*, vol. 498, p. 166192, 2020.

[3] M. K. Verma, N. D. Sharma, S. Sharma, N. Choudhary, and D. Singh, "High magnetoresistance in Lao,gNdogCao,-A, MnO (A= Ca, Li, Na, K) CMR manganites: Correlation between their magnetic and electrical properties," *Materials Research Bulletin*, vol. 125, pp. 10813, 2020;.

[4] S. Biswas, and S. Keshri, "Large magnetocaloric effect near room temperature in $La_{0.67}(Sr, K/Pb)_{0.33}MnO_3$ manganite nanomaterials," *Journal of Materials Science: Materials in Electronics*, vol. 31 pp. 21896-21912, 2020.

[5] L. Joshi, S. S. Rajput, and S. Keshri, "Structural and magneto-transport properties of LCMO–STO composites," *Phase Transitions*, vol. 83, pp. 482, 2010.

[6] H. Nakatsugawa, M. Saito, and Y. Okamoto, "High-temperature thermoelectric properties of perovskite-type $Pr_{0.9}Sr_{0.1}Mn_{1-x}Fe_xO_3$ ($0 \le x \le 1$)," *Journal of Electronic Materials*, vol. 46, pp. 3262-3272, 2017.

[7] C. A. Taboada-Moreno, F. Sánchez-De Jesús, F. Pedro-García, C. A. Cortés-Escobedo, J.A. Betancourt-Cantera, M. Ramírez-Cardona, A. M. Bolarín-Miró, "Large magnetocaloric effect near to room temperature in Sr doped $La_{0.7}Ca_{0.3}MnO_3$," *Journal of Magnetism and Magnetic Materials*, vol. 496, p.165887, 2020.

[8] C. Zener, "Interaction between the d-shells in the transition metals. II. Ferromagnetic compounds of manganese with perovskite structure," *Physical Review*, vol. 82, p. 403, 1951.

[9] T. Endo, T. Goto, Y. Inoue, and Y. Koyama, "Disordered Jahn–Teller-Polaron States in the Simple Perovskite Manganite $Ca_{1-x}La_xMnO_3$ with $0.15 \leqq x \leqq 0.28$," *Journal of the Physical Society of Japan*, vol. 88, p. 074708, 2019.

[10] A. Anshul, S. S. Amritphale, S. Kaur, N. Chandra, A. K. Gupta, and R. Yadav, "Wide-Range Colossal Magnetoresistance in $La_{0.7}A_{0.3}MnO_3$ (A= Sr, Ag) Thin Films," *International Journal of Applied Ceramic Technology*, vol. 9, pp. 214-220, 2012.

[11] G. Channagoudra, A. K. Saw, and V. Dayal, "Low temperature spin polarized tunnelling magneto-resistance in $La_{1-x}Ca_xMnO_3$ (x = 0.375 and 0.625) nanoparticles," *Emergent Materials*, vol. 3, pp. 45-49, 2020.

[12] H. Felhi, M. Smari, R. Hamdi, T. Mnasri, M. Bekri, and E. Dhahri, "Investigation of the Structural, Magnetic, Magnetocaloric, Electrical Properties, and Spin-Polarized Tunneling Effect of the $La_{0.5}Ca_{0.3}Te_{0.2}MnO_3$ System," *Journal of Superconductivity and Novel Magnetism*, vol. 32, pp. 463-473, 2019.

[13] O. Kaman, Z. Jirák, J. Hejtmánek, A. Ndayishimiye, M. Prakasam, and G. Goglio, "Tunneling magnetoresistance of hydrothermally sintered $La_{1-x}Sr_xMnO_3$-silica nanocomposites," *Journal of Magnetism and Magnetic Materials*, vol. 479, pp. 135-143, 2019.

[14] X. Liu, H. Zhu, and Y. Zhang, "Conductive mechanism in manganite materials," *Physical Review B*, vol. 65, p. 024412, 2001.

[15] W. Hizi, H. Rahmouni, M. Gassoumi, K. Khirouni, and S. Dhahri, "Transport properties of $La_{0.9}Sr_{0.1}MnO_3$ manganite," *The European Physical Journal Plus*, vol. 135, no. 6, pp. 1-13, 2020.

[16] R. Thaljaoui, and D. Szewczyk, "Electrical and thermal properties of $Pr_{0.6}Sr_{0.4-x}Ag_xMnO_3$ (x = 0.05 and 0.1) manganite," *Journal of Materials Science*, vol. 55, no. 16, pp. 6761-6770, 2020.

[17] B. Panda, K. L. Routray, and D. Behera, "Studies on conduction mechanism and dielectric properties of the nano-sized $La_{0.7}Ca_{0.3}MnO_3$ (LCMO) grains in the paramagnetic state," *Physica B: Condensed Matter*, vol. 583, p.411967, 2020.

[18] T. M. Tank, M. Prajapat, D. S. Rana, A. Bodhaye, Y. M. Mukovskii, and S. P. Sanyal, "Signature of Ferromagnetic Phase at Low Temperature in Low-Doped $La_{0.88}Ca_{0.12}$ MnO_3 Single Crystal," *Journal of Superconductivity and Novel Magnetism*, vol. 32, no. 10, pp. 3265-3272, 2019.

[19] S. Keshri, and S. S. Rajput, "Effect of BTO addition on the structural and magnetoresistive properties of LSMO," *Phase Transitions*, vol. 87, pp. 136-147, 2014.

[20] R. A. Young, *The Rietveld Method*. New York: Oxford University Press, Inc., 1993.

[21] FullProf Suite. https://www.ill.eu/sites/fullprof/

[22] L. S. Ewe, A. Jemat, K. P. Lim, and R. Abd-Shukor, "Electrical, magnetoresistance and magnetotransport properties of $Nd_{1-x}Sr_xMnO_3$," *Physica B: Condensed Matter*, vol. 416, pp. 17-22, 2013.

[23] M. Gupta, R. K. Kotnala, W. Khan, A. Azam, and A. H. Naqvi, "Magnetic, transport and magnetoresistance behavior of Ni doped $La_{0.67}Sr_{0.33}Mn_{1-x}Ni_xO_3$ ($0.00 \leq x \leq 0.09$) system," *Journal of Solid State Chemistry*, vol. 204, pp. 205-212, 2013.

[24] P. R. Sagdeo, S. Anwar, N. P. Lalla, "Powder X-ray diffraction and Rietveld analysis of $La_{1-x}Ca_xMnO_3$ ($0 < x < 1$)," *Powder Diffraction*, vol. 21, pp. 40-44, 2006.

[25] M. S. Islam, D. T. Hanh, F. A. Khan, M. A. Hakim, D. L. Minh, N. N. Hoang, N. H. Hai, and N. Chau, "Giant magneto-caloric effect around room temperature at moderate low field variation in $La_{0.7}(Ca_{1-x}Sr_x)_{0.3}MnO_3$ perovskites," *Physica B: Condensed Matter*, vol. 404, pp. 2495-2498, 2009.

[26] Z. Chen, T. A. Tyson, K. H. Ahn, Z. Zhong and J. Hu, "Origin of the non-linear pressure effects in perovskite manganites: Buckling of Mn-O-Mn bonds and Jahn-Teller distortion of the MnO_6 octahedra induced by pressure," *Journal of Magnetism and Magnetic Materials*, vol. 322, pp. 3049-3052, 2010.

[27] W. J. Lu, X. Luo, C. Y. Hao, W. H. Song, and Y. P. Sun, "Magnetocaloric effect and Griffiths-like phase in $La_{0.67}Sr_{0.33}$ MnO_3 nanoparticles," *Journal of Applied Physics*, vol. 104, pp. 113908, 2008.

[28] M. Oumezzine, S. Kallel, O. Peña, N. Kallel, T. Guizouarn, F. Gouttefangeas, and M. Oumezzine, "Correlation between structural, magnetic and electrical transport properties of barium vacancies in the $La_{0.67}Ba_{0.33-x}MnO_3$ (x = 0, 0.05, and 0.1) manganite," *Journal of Alloys and Compounds*, vol. 582, pp. 640-646, 2014.

[29] L. Yang, Q. Duanmu, L. Hao, X. Wang, Y. Wei, Z. Zhang, and H. Zhu, "Structural, magnetic and electrical properties of double-doped manganites $Y_{0.5+y}Sr_{0.5-y}Mn_{1-y}Cr_yO_3$ ($0 \leq y \leq 0.5$)," *Journal of Magnetism and Magnetic Materials*, vol. 341, pp. 30-35, 2013.

[30] M. Nasri, M. Triki, E. Dhahria, E. K. Hlil, and P. Lachkar, "Electrical transport and magnetoresistance properties of $(1-x)La_{0.6}Sr_{0.4}MnO_3/x(Sb_2O_3)$ composites," *Journal of Alloys and Compounds*, vol. 576, pp. 404-408, 2013.

[31] S. Keshri, L. Joshi, and S. S. Rajput, "Studies on $La_{0.67}Ca_{0.33}$ MnO_3–$SrTiO_3$ composites using two-phase model," *Journal of Alloys and Compounds*, vol. 509, pp. 5796-5803, 2011.

[32] M. Rubinstein, "Two-component model of polaronic transport," *Journal of Applied Physics*, vol. 87, pp. 5019-5021, 2000.

[33] N. Panwar, D. K. Pandya, A. Rao, K .K. Wu, N. Kaurav, Y. K. Kuo, and S. K. Agarwal, "Electrical and thermal properties of $Pr_{2/3}(Ba_{1-x}Cs_x)_{1/3}MnO_3$ manganites." *The European Physical Journal B*, vol. 65, pp. 179-186, 2008.

[34] N. F. Mott, and E. A. Davis, *Electronic Processes in Non–Crystalline Materials*. New York: Oxford University Press, Inc., 1979.

[35] K. Sega, Y. Kuroda, and H. Sakata, "Dc conductivity of V_2O_5–MnO–TeO_2 glasses," *Journal of materials science*, vol. 33, pp. 1303-1308, 1998.